GLT1 activity and immunoblotting

Levels of GLT1 protein were quantified by immunoblots[3]. Functional glutamate transport was measured by accumulation of ^{3}H-glutamate in spinal cord slice or crude cortical synaptosomal membranes[25]. Measurement of total glutamate uptake actually reflects the combined physiological activity of all transporter subtypes. GLT1 protein is uniquely sensitive to transport inhibition by dihydrokainate (DHK). To estimate the contribution of GLT1 to transport, aliquots of tissue homogenates were also incubated with 300 μM DHK. Non-specific uptake was determined in the presence of 300 μM *threo*-β-hydroxyaspartate (THA), at 0 °C and in sodium-free homogenates.

Generation of GLT1 BAC eGFP transgenic mouse

The BAC transgenic mice were generated as described previously[26] with a shuttle vector provided by N. Heintz. The BAC clone included approximately 45 kb upstream of the first GLT1 exon, the full GLT1 coding region (123 kb) and 24 kb downstream of the last exon. EGFP cDNA was inserted into the GLT1 start codon.

Oxygen glucose deprivation/ischaemic preconditioning

Primary cortical mixed neuronal-glial cell cultures were prepared from rodent fetal cortex (gestation day 14–16 CD1 mice) using the paradigm of ischaemic preconditioning[18].

Motor neuron toxicity

Neuroprotection in spinal cord organotypic cultures prepared from postnatal day 8–9 wild-type rat or GLT1-null mouse tissue was performed as described previously[11]. Ceftriaxone was added for 5–7 days before the addition of 100 μM THA or DL-*threo*-β-benzyloxyaspartate, (TBOA) 100 μM. Surviving motor neurons were counted 2–3 weeks later by staining for phosphorylated neurofilaments (SMI-32).

G93A SOD1 mouse—disease onset and survival

Male transgenic mice expressing the human G93A SOD1 (B6SJL-TgN(SOD1-G93A)1Gur, high expressor) were bred with background-matched B6SJL wild-type females (Jackson Laboratories). The progeny were genotyped and used for subsequent studies. Experiments were conducted at Psychogenics (Hawthorne, New York) in accordance with protocols approved by the Johns Hopkins Animal Care and Use Committee. Mice were assessed by daily observation for survival, and by weekly weighing and testing of grip strength starting at 12 weeks of age[22,23]. All experiments were performed blinded with coded syringes for injection.

Histology and motor neuron counts

Mice were perfused via cardiac infusion with 4% buffered paraformaldehyde and spinal cord post fixed with the same solution. The lumbar enlargement was collected, paraffin embedded, and serially sectioned at 14 μm, for a total of 140 sections. Every seventh section was stained with haematoxylin and eosin, and examined at 20 × for motor neuron identification and counting[22]. Images were acquired using the Zeiss LSM 510 Meta confocal microscope (argon laser setting at 488 nm) with the operator blinded to treatment groups. All images were captured with the same gain, offset, pinhole diameter (2.53 Airy units), and scan speed (12.8 μs with scan averaging set to 2). Z-series images were collected at 1.03 μm intervals.

Statistics

Quantitative differences between *in vitro* and *in vivo* drug effects were analysed by analysis of variance (ANOVA) or Students *t*-test. Survival analysis was performed by Kaplan-Meier analysis. Software for statistics included Statview, and JMP 5.1 (SAS Software).

Received 11 July; accepted 4 November 2004; doi:10.1038/nature03180.

1. Rothstein, J. D. *et al.* Knockout of glutamate transporters reveals a major role for astroglial transport in excitotoxicity and clearance of glutamate. *Neuron* **16,** 675–686 (1996).
2. Danbolt, N. C. Glutamate uptake. *Prog. Neurobiol.* **65,** 1–105 (2001).
3. Rothstein, J. D., Van Kammen, M., Levey, A. I., Martin, L. J. & Kuncl, R. W. Selective loss of glial glutamate transporter GLT-1 in amyotrophic lateral sclerosis. *Ann. Neurol.* **38,** 73–84 (1995).
4. Rao, V. L. *et al.* Antisense knockdown of the glial glutamate transporter GLT-1, but not the neuronal glutamate transporter EAAC1, exacerbates transient focal cerebral ischemia-induced neuronal damage in rat brain. *J. Neurosci.* **21,** 1876–1883 (2001).
5. Ye, Z. C., Rothstein, J. D. & Sontheimer, H. Compromised glutamate transport in human glioma cells: reduction-mislocalization of sodium-dependent glutamate transporters and enhanced activity of cystine-glutamate exchange. *J. Neurosci.* **19,** 10767–10777 (1999).
6. Sepkuty, J. P. *et al.* A neuronal glutamate transporter contributes to neurotransmitter GABA synthesis and epilepsy. *J. Neurosci.* **22,** 6372–6379 (2002).
7. Su, Z. Z. *et al.* Insights into glutamate transport regulation in human astrocytes: cloning of the promoter for excitatory amino acid transporter 2 (EAAT2). *Proc. Natl Acad. Sci. USA* **100,** 1955–1960 (2003).
8. Goodman, L. S., Hardman, J. G., Limbird, L. E. & Gilman, A. G. *Goodman & Gilman's The Pharmacological Basis of Therapeutics* (McGraw-Hill Medical Pub. Division, New York, 2001).
9. Tanaka, K. *et al.* Epilepsy and exacerbation of brain injury in mice lacking the glutamate transporter GLT-1. *Science* **276,** 1699–1702 (1997).
10. Watase, K. *et al.* Motor discoordination and increased susceptibility to cerebellar injury in GLAST mutant mice. *Eur. J. Neurosci.* **10,** 976–988 (1998).
11. Rothstein, J. D., Jin, L., Dykes-Hoberg, M. & Kuncl, R. W. Chronic inhibition of glutamate uptake produces a model of slow neurotoxicity. *Proc. Natl Acad. Sci. USA* **90,** 6591–6595 (1993).
12. Chandrasekar, P., Rolston, K., Smith, B. & LeFrock, J. Diffusion of ceftriaxone into the cerebrospinal fluid of adults. *J. Antimicrob. Chemother.* **14,** 427–430 (1984).
13. Nau, R. *et al.* Passage of cefotaxime and ceftriaxone into cerebrospinal fluid of patients with uninflamed meninges. *Antimicrob. Agents Chemother.* **37,** 1518–1524 (1993).
14. Kazragis, R., Dever, L., Jorgensen, J. & Barbour, A. *In vivo* activities of ceftriaxone and vancomycin against Borrelia spp. in the mouse brain and other sites. *Antimicrob. Agents Chemother.* **38,** 2632–2636 (1996).
15. Chen, W. *et al.* Expression of a variant form of the glutamate transporter GLT1 in neuronal cultures and in neurons and astrocytes in the rat brain. *J. Neurosci.* **22,** 2142–2152 (2002).
16. Schlag, B. D. *et al.* Regulation of the glial Na^+-dependent glutamate transporters by cyclic AMP analogs and neurons. *Mol. Pharmacol.* **53,** 355–369 (1998).
17. Guo, H. *et al.* Increased expression of the glial glutamate transporter EAAT2 modulates excitotoxicity and delays the onset but not the outcome of ALS in mice. *Hum. Mol. Genet.* **12,** 2519–2532 (2003).
18. Romera, C. *et al. In vitro* ischemic tolerance involves upregulation of glutamate transport partly mediated by the TACE/ADAM17-tumor necrosis factor-alpha pathway. *J. Neurosci.* **24,** 1350–1357 (2004).
19. Spalloni, A. *et al.* Cu/Zn-superoxide dismutase (GLY93 → ALA) mutation alters AMPA receptor subunit expression and function and potentiates kainate-mediated toxicity in motor neurons in culture. *Neurobiol. Dis.* **15,** 340–350 (2004).
20. Canton, T. *et al.* RPR 119990, a novel alpha-amino-3-hydroxy-5-methyl-4-isoxazolepropionic acid antagonist: synthesis, pharmacological properties, and activity in an animal model of amyotrophic lateral sclerosis. *J. Pharmacol. Exp. Ther.* **299,** 314–322 (2001).
21. Rothstein, J. D. & Kuncl, R. W. Neuroprotective strategies in a model of chronic glutamate-mediated motor neuron toxicity. *J. Neurochem.* **65,** 643–651 (1995).
22. Kaspar, B. K., Llado, J., Sherkat, N., Rothstein, J. D. & Gage, F. H. Retrograde viral delivery of IGF-1 prolongs survival in a mouse ALS model. *Science* **301,** 839–842 (2003).
23. Drachman, D. B. *et al.* Cyclooxygenase 2 inhibition protects motor neurons and prolongs survival in a transgenic mouse model of ALS. *Ann. Neurol.* **52,** 771–778 (2002).
24. Howland, D. S. *et al.* Focal loss of the glutamate transporter EAAT2 in a transgenic rat model of SOD1 mutant-mediated amyotrophic lateral sclerosis (ALS). *Proc. Natl Acad. Sci. USA* **99,** 1604–1609 (2002).
25. Rothstein, J. D., Martin, L. J. & Kuncl, R. W. Decreased glutamate transport by the brain and spinal cord in amyotrophic lateral sclerosis. *N. Engl. J. Med.* **326,** 1464–1468 (1992).
26. Gong, S., Yang, X. W., Li, C. & Heintz, N. Highly efficient modification of bacterial artificial chromosomes (BACs) using novel shuttle vectors containing the R6Kgamma origin of replication. *Genome Res.* **12,** 1992–1998 (2002).

Supplementary Information accompanies the paper on **www.nature.com/nature**.

Acknowledgements We are grateful to J. Lee and C. Cocci for technical assistance; K. Tanaka for GLT1-null mice; C. Leahy for ALS mouse studies; and J. Heemskerk for initiating the project, discussions and encouragement. G93A SOD1 mice were provided by Project ALS. The work was supported by the NIH, the Muscular Dystrophy Association and The Robert Packard Center for ALS Research at Johns Hopkins.

Competing interests statement The authors declare competing financial interests: details accompany the paper on **www.nature.com/nature**.

Correspondence and requests for materials should be addressed to J.D.R. (jrothste@jhmi.edu).

Nucleolar proteome dynamics

Jens S. Andersen[1]†, Yun W. Lam[2]†, Anthony K. L. Leung[2]*, Shao-En Ong[1], Carol E. Lyon[2], Angus I. Lamond[2] & Matthias Mann[1]

[1]*Department of Biochemistry and Molecular Biology, Campusvej 55, DK-5230 Odense M, Denmark*
[2]*Wellcome Trust Biocentre, MSI/WTB Complex, University of Dundee, Dundee DD1 4HN, UK*

* Present address: Center for Cancer Research, Department of Biology, Massachusetts Institute of Technology, Cambridge, Massachusetts 02139, USA
† These authors contributed equally to this work

The nucleolus is a key organelle that coordinates the synthesis and assembly of ribosomal subunits and forms in the nucleus around the repeated ribosomal gene clusters. Because the production of ribosomes is a major metabolic activity, the function of the nucleolus is tightly linked to cell growth and proliferation, and recent data suggest that the nucleolus also plays an important role in cell-cycle regulation, senescence and stress responses[1–4]. Here, using mass-spectrometry-based organellar proteomics and stable isotope labelling[5], we perform a quantitative analysis of the proteome of human nucleoli. *In vivo* fluorescent imaging techniques are directly compared to endogenous protein changes measured by proteomics. We characterize the flux of 489 endogenous nucleolar proteins in response to three different metabolic inhibitors that each affect nucleolar morphology.

Proteins that are stably associated, such as RNA polymerase I subunits and small nuclear ribonucleoprotein particle complexes, exit from or accumulate in the nucleolus with similar kinetics, whereas protein components of the large and small ribosomal subunits leave the nucleolus with markedly different kinetics. The data establish a quantitative proteomic approach for the temporal characterization of protein flux through cellular organelles and demonstrate that the nucleolar proteome changes significantly over time in response to changes in cellular growth conditions.

HeLa cell nucleoli were isolated in high purity by density gradient fractionation[6]. Analysis of isolated nucleoli by electron microscopy shows that they remain intact and preserve the internal morphology seen *in situ* (Supplementary Fig. 1a, b). The preparations are homogeneous with virtually all particles visible by electron microscopy corresponding to nucleoli (Supplementary Fig. 1c and other data not shown). The isolated nucleoli retain transcriptional activity, as determined by 5-bromo-UTP (Br-UTP) incorporation (Supplementary Fig. 1d). The inhibition of transcription caused by actinomycin D treatment was confirmed by 5-fluorouridine incorporation analysis of control and actinomycin D-treated HeLa cells (Supplementary Fig. 1e, f).

Protein mixtures from individual one-dimensional gel slices were in gel digested with either trypsin or endoproteinase Lys-C. The resulting peptide mixtures were analysed in several runs of nano-scale liquid chromatography—tandem mass spectrometry (LC MS/MS) on an ion trap—Fourier Transform mass spectrometer, capable of very high mass accuracy and of sequencing several peptides per second (see Methods). To reduce false positives caused by random impurities, we independently prepared nucleoli in our two laboratories and only included proteins identified in both preparations in the final proteome. Tandem mass spectra were searched in the human sequence database, considering only peptides conforming to full trypsin or Lys-C specificity and whose mass matched the calculated mass within 3 p.p.m. (see Methods). Approximately 11,130 unique peptide sequences were unambiguously matched to human genes with an average mass accuracy of 0.7 p.p.m. (see Supplementary Table 1). These peptides were used to identify proteins in the purified nucleoli with high stringency, requiring at least two high-scoring peptides per protein (see Supplementary Table 1). Under these conditions, we estimate a false positive rate for protein identification below 0.1% (see Methods).

We compared this expanded nucleolar proteome with published information on proteins localized to the nucleolus in budding yeast from a recent large-scale study of yeast protein localization using green fluorescent protein (GFP) fusion proteins[7]. Out of the 142 yeast nucleolar proteins that have at least one human homologue, 124 are found in the updated nucleolar proteome (87%). In our previous study[8], ~58% of the yeast homologues were present in the proteome of 271 human factors. A comparison of the increasing fraction of the human homologues of yeast nucleolar proteins found in each separate determination of the HeLa cell nucleolar proteome during the past two years suggests that detection levels are approaching saturation coverage, at least with the technology currently available (Fig. 1b). The data indicate that approximately 90% of the yeast nucleolar proteins with human homologues are also nucleolar components in HeLa cells and that the nucleolus is highly conserved throughout the eukaryotic kingdom.

Werner's syndrome protein, which was not sequenced at all in our previous study, was here detected with six different peptides, demonstrating that the combination of increased sensitivity,

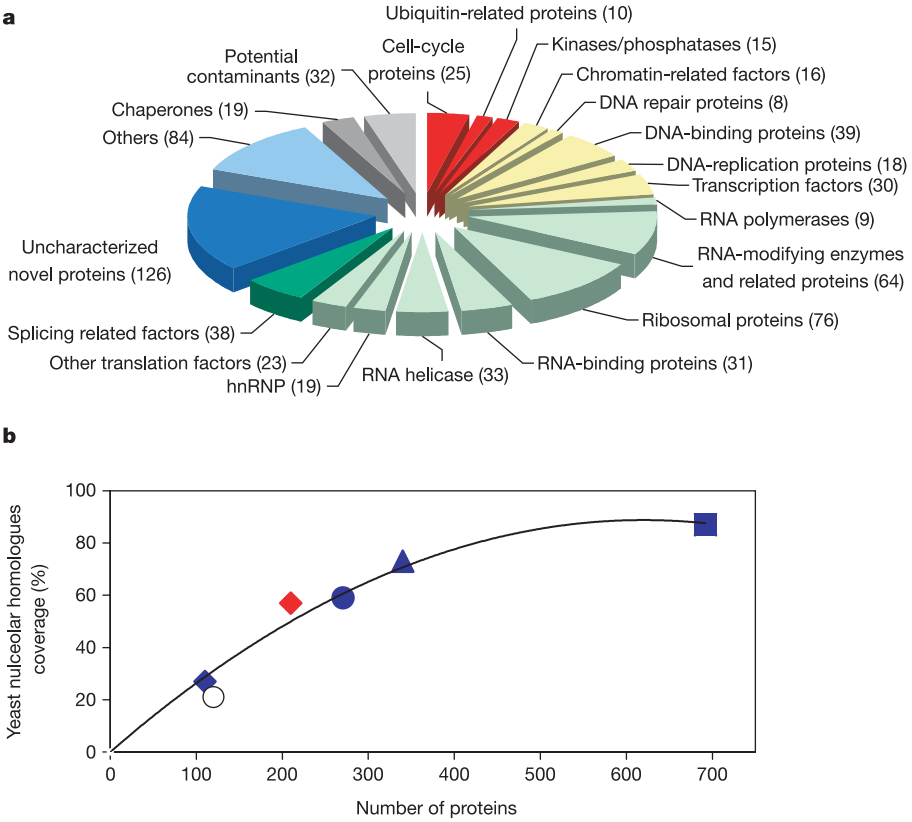

Figure 1 The nucleolar proteome. **a**, Classification of nucleolar proteins by functional category. Numbers indicate identified proteins in each category. **b**, Coverage of human homologues of yeast nucleolar proteins in different data sets. Open circle, proteins annotated as nucleolar in the literature; blue diamond, MALDI study in ref. 8; red diamond, LC MS/MS study from ref. 30; blue circle, all proteins from ref. 8; blue triangle, LC MS/MS with QSTAR (this study); blue square, LTQ-FT data (this study).

resolution and peptide sequencing speed achieved much greater sequencing depth. Regulatory proteins in the nucleolar proteome included casein kinase II and the phosphatase PP1, which may have roles in nucleolar regulation[9,10], and protein kinases CDK2, CDK7, CDK9, CDC2L5, Cip1/p21 interacting protein and Aurora B, which are involved in controlling cell-cycle progression. We also observed key regulators of p53, such as p14ARF, and the Ser/Thr protein kinases VRK1 and ATM, which were reported to be sequestered in the nucleolus. Nonetheless, there remain some proteins previously reported to reside in the nucleolus that were not detected, such as the transcription factor RRN3 (ref. 11) and gemin 4 (ref. 12), which is a component of the survival of motor neuron (SMN) complex. Possible reasons for their continued absence from the observed proteome could include that they are present in exceedingly small amounts, or are not associated sufficiently stably with nucleoli to be isolated using the purification methods available. The data set from all our nucleolar mass spectrometry analyses defines an updated group of 692 proteins that reproducibly copurify with human nucleoli (also available in a searchable online database at http://www.lamondlab.com/NOPdb/). Bioinformatic classification (Fig. 1a) demonstrates functional diversity of the nucleolar proteome and the presence of approximately one-third of proteins with no previous functional information. Note that many proteins that stably copurify with nucleoli are also present at other cellular locations and some only accumulate transiently in nucleoli. The proteins identified included a minor fraction of potential contaminants, which have been included for completeness but are marked in Supplementary Table 1.

Unlike cytosolic organelles, nuclear bodies are not membrane bound and the principles of their organization and assembly are not well understood[13]. Recent light microscopy studies, analysing nuclear fluorescent fusion proteins using techniques such as fluorescence recovery after photobleaching (FRAP) or fluorescence loss in photobleaching (FLIP), have revealed the high mobility of many nuclear factors and their often rapid exchange between nuclear bodies and the surrounding nucleoplasm[14,15]. Temporal studies have uncovered evidence for maturation pathways in which nuclear factors can transit between different nuclear bodies in a defined sequence[16]. To evaluate in a comprehensive and quantitative approach how dynamic the nucleolar proteome may be, we performed a series of proteomic studies on nucleoli isolated either from control cells, or from cells treated with drugs that inhibit transcription or protein degradation. We used stable-isotope labelling by amino acids in cell culture (SILAC)[17] to characterize the response of the nucleolar proteome to transcription inhibition (Fig. 2). A HeLa cell line was metabolically labelled with either normal arginine ($^{12}C_6{}^{14}N_4$-Arg, termed here Arg0), carbon substituted arginine ($^{13}C_6{}^{14}N_4$-Arg, termed here Arg6) or carbon plus nitrogen substituted arginine ($^{13}C_6{}^{15}N_4$-Arg, termed here Arg10) respectively. This 'triple encoding' procedure allows three cell states to be measured in one experiment[18]. The cells are identical in all respects except that peptides derived after proteolytic digestion of the proteins can be distinguished in the mass spectrometer by their offsets of either zero, six or ten mass units.

The three HeLa cell populations were treated with actinomycin D at a final concentration of 1 $\mu g\,ml^{-1}$, which inhibits transcription by RNA polymerase I, II and III[19] for different lengths of time. A decrease in RNA synthesis levels, assayed by Br-UTP incorporation, was detected within 15–30 min, reflecting the time required for drug uptake by the cells (data not shown). Next, equal amounts of cells from each time point were mixed and nucleoli isolated directly from this mixed cell pool (Fig. 2a). Nucleolar proteins were fractionated and analysed by LC MS/MS as before. Because every arginine-containing tryptic peptide occurs in three isotopic forms, the intensities of these three mass spectrometry peaks directly reveal the relative ratios of the corresponding protein in the nucleolus at each of the three time points. Typically, several peptides per protein are quantified (see Methods and Supplementary Table 2). Figure 2b, c shows representative mass spectra for peptides derived from p68. The increased peak heights for the 20 (Arg6) and 80 (Arg10) minute time points show that p68 is recruited to the nucleolus (Fig. 2d).

The kinetic experiments were performed using the HeLa$^{YFP-p68}$ cell line[8], allowing a direct comparison of changes in the level of YFP–p68 determined either by this proteomic analysis, or *in vivo* by digital fluorescence microscopy (Fig. 3). Western blotting analysis showed that the ratio between the yellow fluorescent protein (YFP)-tagged and untagged, endogenous p68 in isolated nucleoli remained the same during actinomycin D treatment and that both similarly increased in nucleoli when transcription was blocked (Fig. 3a). We monitored by microscopy the YFP–p68 fluorescence signal in nucleoli of live HeLa$^{YFP-p68}$ cells following actinomycin D treatment and compared these *in vivo* data with the SILAC measurements of YFP–p68 in isolated nucleoli after actinomycin D treatment (Fig. 3b, c). Similar relative changes in nucleolar p68 levels were measured by both techniques (Fig. 3c and other data not shown). There was no overall change in the total cellular YFP–p68 fluorescence level following actinomycin D treatment, demonstrating that the increased nucleolar p68 fluorescence results from the intranuclear redistribution of p68 (Fig. 3c). A similar close agreement of fluorescence and SILAC data was also seen for two additional cell lines analysed that stably express either YFP-tagged fibrillarin (Fig. 3d) or YFP-tagged ribosomal protein L27 (Fig. 3e). Although it is possible that some changes in protein levels could occur after blocking transcription, we don't expect this to have a major effect on nucleolar proteome dynamics during the 2 h time course of transcription inhibition tested because most mammalian messenger

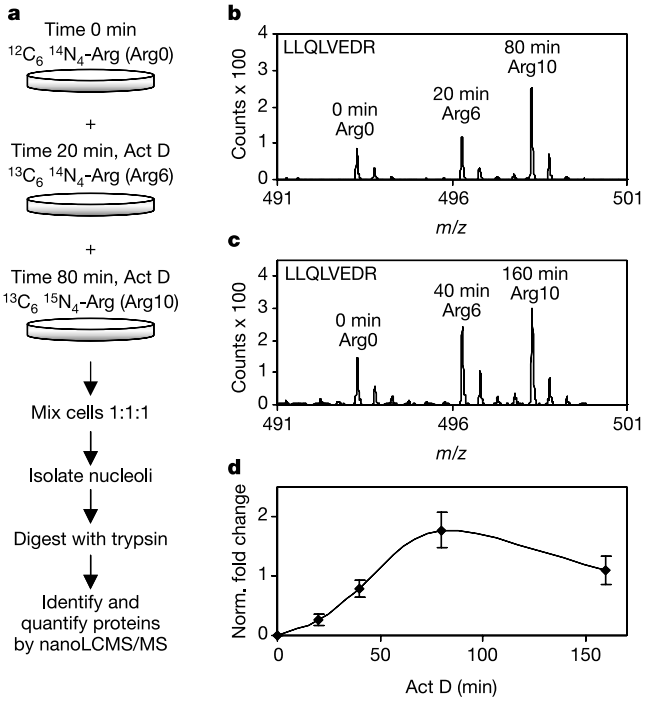

Figure 2 Determination of nucleolar protein dynamics. **a**, The proteomes in three cell populations are encoded by incorporation of stable isotope derivatives of arginine (SILAC method). Cells are metabolically labelled with Arg0, Arg6 and Arg10 for at least five cell doublings and are then treated for 0, 20 and 80 min, respectively. Cells are mixed and nucleoli purified and analysed by mass spectrometry. The analysis is repeated with a common zero point and additional time points of transcription inhibition to achieve higher time resolution. **b**, **c**, Spectra of peptides of p68, indicating increasing amounts p68 recruited to the nucleolus. **d**, Dynamic profiles of p68. Y axis is in units of normalized fold change of p68. Error bars are s.d. from several p68 peptides.

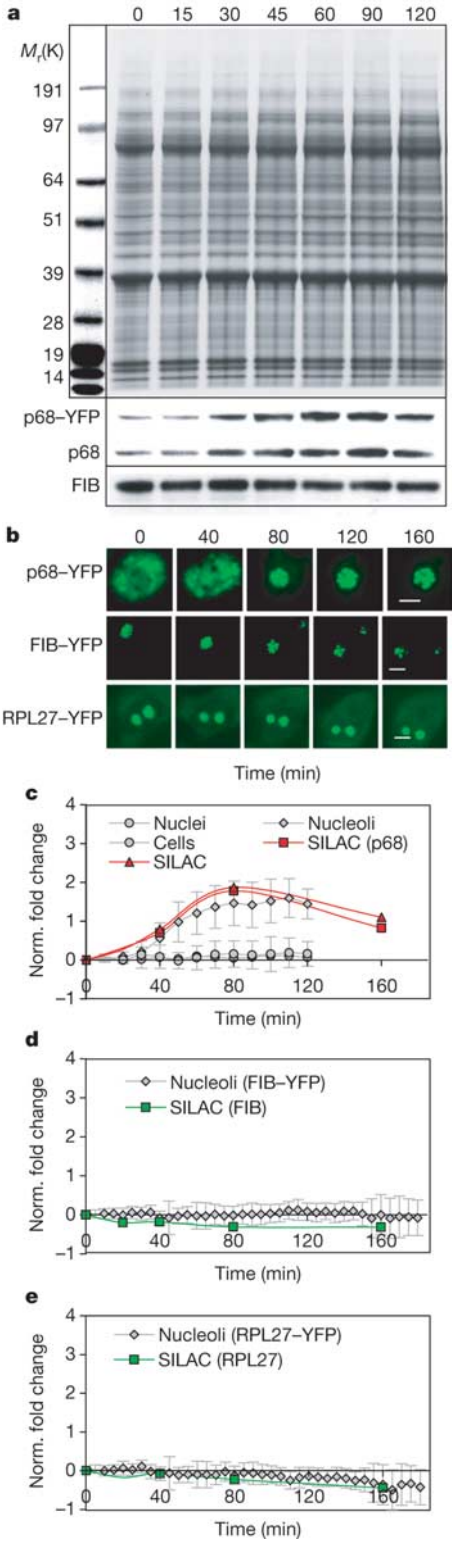

Figure 3 Comparison of different methods to measure nucleolar protein dynamics. **a**, Proteins from nucleoli isolated from HeLa YFP–p68 cells treated with actinomycin D (1 μg ml^{-1}) for 0–120 min were probed with antibodies (see Methods). **b**–**e**, Live HeLa cells stably expressing YFP–p68, YFP–fibrillarin (FIB) and YFP–RPL27 were treated with actinomycin D (1 μg ml^{-1}) and imaged for at least 120 min. The changes in the intranucleolar YFP fluorescence signals (grey curves) were compared to the changes in levels of the corresponding endogenous proteins detected in isolated nucleoli by SILAC (red or green curves); the YFP–p68 protein was also detected by SILAC. Scale bars, 3 μm. Error bars are s.d. from fluorescence measurements on five individual cells in each case.

RNAs have a half-life greater than 6 h (ref. 20). As illustrated for all three proteins tested, the changes in protein levels in nucleoli result primarily from redistribution. In addition, it was possible to resolve separate peptides from the YFP-tagged p68 and the endogenous untagged p68 proteins, allowing a comparison of their kinetic profiles in response to actinomycin D (Fig. 3c). Importantly, both show a similar kinetic response, indicating that the presence of the YFP tag does not significantly alter the dynamic behaviour of p68. Thus, the combination of mass spectrometry and fluorescence kinetic data measurements offers a powerful new way to validate these cell lines as model systems for *in vivo* studies of nucleolar dynamics.

Within the detected nucleolar proteome, 489 proteins produced peptides that allowed SILAC analysis. The relative levels of all 489 factors were therefore quantified in two large-scale experiments, measured at five or nine separate time points after inhibiting transcription with actinomycin D (Supplementary Table 2). The data show good reproducibility between the two experiments (Fig. 4 and see below). We observed a wide range of responses to actinomycin D treatment for different proteins (Fig. 4). The steady-state levels of many nucleolar proteins decreased to various extents on actinomycin D treatment. Factors known to be depleted from the nucleolus upon transcription inhibition (for example, PTB, Ki-67, GU and NOH61) were also found to decrease in our data set (Fig. 4b). Factors depleted from nucleoli after actinomycin D treatment included ribosomal proteins, RNA processing factors, exosome components and RNA polymerase I (Fig. 4a). This probably reflects the export of assembled ribosomal subunits taking place without ongoing RNA polymerase I activity to synthesize new ribosomal RNA substrate, and suggests that the association of many components with the nucleolus is dependent on ribosome subunit synthesis. A subset of proteins accumulated within nucleoli after transcription had been arrested, including all 11 proteins we identified previously to accumulate in nucleoli after actinomycin D treatment[8]. Remarkably, the level of some proteins increased up to tenfold (Fig. 4a). This result suggests that the nucleolus is not a simple ribosome synthesis machine that progressively breaks down in the absence of transcription. Instead, transcription inhibition leads to a more subtle redistribution of nuclear proteins, and the partition of proteins between the nucleolus and nucleoplasm may reflect the general physiological status of the cell.

Different nucleolar factors show major differences in their kinetics, of either decrease or accumulation. For example, separate nucleolar members of the DEAD box helicase family, which are likely to have distinct and non-overlapping functions in the nucleolus, respond to transcription inhibition with different kinetics (Fig. 4c). In contrast, separate subunits of RNA polymerase I, which physically associate in a stable protein complex, each leave nucleoli at an almost identical rate (Fig. 4d). These data are consistent with RNA polymerase I proteins moving coordinately, either as part of stable complexes or through the actions of common receptors. Similarly, separate small nuclear ribonucleoprotein particle (snRNP) proteins accumulate within nucleoli at identical rates, consistent with their association in a stable RNP complex. Multiple protein components of the exosome and the RNase P complex each also showed coordinate kinetics (Fig. 4e). Whereas multiple components appear to accumulate within the nucleolus only in the presence of rRNA substrate, the fact that many other proteins either remain at similar levels, or even increase within nucleoli after transcription inhibition, indicates that not all resident nucleolar proteins are dependent upon rRNA substrate synthesis. Thus the data do not support the view that the nucleolus is a transient structure formed only as a result of ongoing rRNA synthesis and indicate that at least a core of the nucleolar proteins remain associated in the absence of nascent rRNA transcription and ribosomal subunit assembly. The protein components of the large and small ribosomal subunits leave nucleoli with markedly different

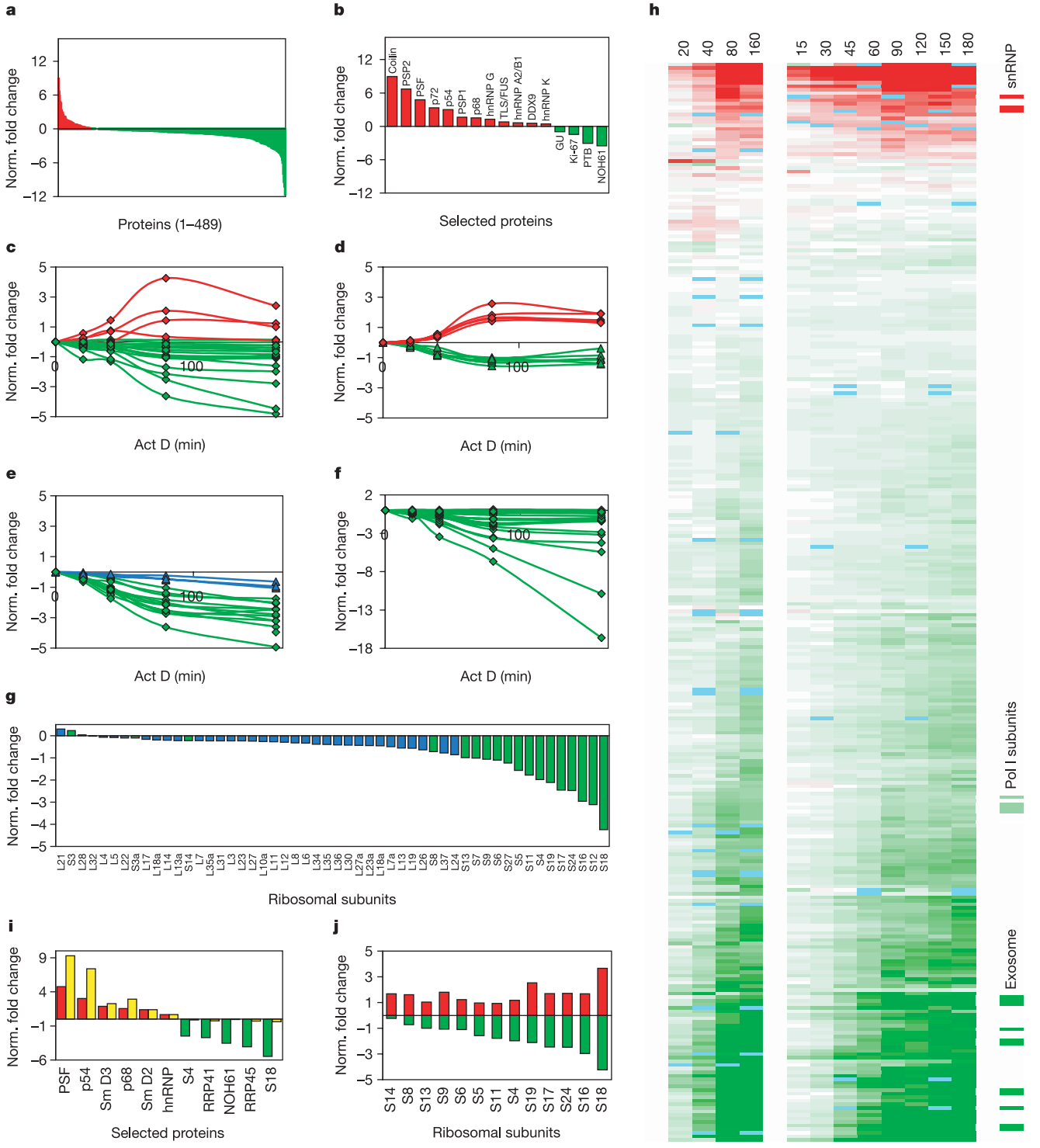

Figure 4 Dynamic profiles of nucleolar proteins. Red indicates recruited proteins and green indicates depleted proteins. **a**, All proteins showing change from first to last time points. **b**, Proteins known from the literature to be recruited to or depleted from nucleoli upon treatment with actinomycin D (Act D). **c**, Different kinetic profiles for different DEAD box proteins (top curve to bottom curve, see Supplementary Table 2: BAT1, CHD4, DDX10, DDX17, DDX18, DDX21, DDX24, DDX27, DDX31, DDX3X, DDX48, DDX49, DDX5, DDX50, DDX51, DDX52, DDX54, DDX56, DHX33, DHX37, MTR4, RUVBL2). **d**, Dynamic profile for polymerase I subunits (green; POLR1C, PAF53, POLR1B, POLR1A, POLR1D, TTF1, UBTF) and snRNP proteins (red; SNRPB, SNRPA, SNRPD2, SNRPD3, SNRPF). **e**, Dynamic profiles for subunits of the exosome (green; RRP42, RRP46, RRP40, RRP4, RRP43, RRP41, RRP45, CSL4, RRP44, MTR3, MTR4) and the RNase P (blue; RPP14, RPP25, RPP38, RPP30, POP1). **f**, Dynamic profile of the human homologues of the yeast SSU processome proteins. **g**, Fold change of the large (blue) and small (green) ribosomal subunit proteins. **h**, Hierarchical clustering of 302 proteins using fold change data from Supplementary Table 2 (five and nine time point experiments). The indicated proteins are snRNP (SNRPA, SNRPD2, SNRPD3), Pol I (POLR1A, POLR1D, POLR1B, POLR1C) and exosome components. See Supplementary Fig. 2 for protein names. **i**, Comparison of fold change for a subset of proteins upon treatment with actinomycin D (red/green, average fold change after treatment for 80 and 160 min) and DRB (yellow, 80 min). **j**, Comparison of fold change for the small ribosomal subunit proteins upon treatment with actinomycin D (green) and MG132 (red, 8 h).

kinetics (Fig. 4g), consistent with previous reports that biogenesis and nuclear export of the large and small ribosomal subunits occur independently in budding yeast[21]. The variation in kinetics for different ribosomal proteins probably occurs because ribosome subunit assembly is a complex, multi-step process and not all the factors assemble on the rRNAs simultaneously. The dynamic profile of the human homologues of the yeast small-subunit (SSU) processome[22], which is involved in the biogenesis of the 40S preribosomal subunit, displayed some of the most marked changes, decreasing by 10–15-fold in abundance within nucleoli after actinomycin D treatment (Fig. 4f). These data indicate that at least a subset of the processome components (homologues of Sof1, Upt11, Upt6, Upt7 and Upt14) are strongly dependent upon rRNA expression for their accumulation within nucleoli. We infer that these factors are specifically recruited into nucleoli to participate in ribosome subunit biogenesis and are not retained within nucleoli under conditions when no new rRNA substrate is being transcribed.

Figure 4h shows that changes in protein levels brought about by either recruitment to or loss from an organelle can be visualized and analysed by hierarchical clustering in a similar manner to the visualization of expression changes in microarray experiments[23]. Inspection of the graph indicates reproducibility between patterns of the five and nine time point experiments. Groups of strongly recruited and depleted proteins clearly show the same pattern in both experiments (top and bottom clusters in Fig. 4h). Furthermore, functional and/or structural protein complexes such as the snRNPs, Pol I subunits and exosome cluster in tight regions (indicated in the rightmost column).

We repeated the kinetic analysis with different inhibitors that also affect nucleolar morphology. Treatment with 5,6-dichlorobenzimidazole riboside (DRB), which selectively inhibits RNA polymerase II but not polymerase I (ref. 24), resulted in nucleolar accumulation of a similar set of proteins to those seen in actinomycin D treatment (Fig. 4i and other data not shown). However, DRB caused fewer proteins to decrease in nucleolar abundance. Notably, the large and small ribosomal subunit proteins and components of the exosome remained relatively unchanged after DRB treatment. This supports the view that the decrease in ribosomal proteins and some other factors following inhibition of RNA polymerase I activity is caused, at least in part, by the export of ribosome subunits in the absence of new rRNA synthesis. We infer also that the accumulation of proteins in nucleoli following transcription inhibition results primarily from a block of RNA polymerase II activity.

Finally, we treated cells with the proteasome inhibitor MG132, which affects nucleolar morphology but does not directly inhibit RNA polymerase activity[25]. A SILAC experiment was performed on HeLa$^{YFP–p68}$ cells treated for up to 16 h with MG132 at a final concentration of 10 μM. Quantitative proteomics showed that MG132 also caused a major change in the nucleolar proteome, but largely affected a different set of proteins as compared with inhibitors of transcription (Fig. 4j). MG132 caused a striking increase in the levels of ribosomal proteins in the isolated nucleoli, particularly in the case of small ribosomal subunit proteins, which contrasts with the general decrease in ribosomal proteins in nucleoli caused by actinomycin D. The reason for this unexpected effect is unclear but may reflect a novel regulatory link between ribosome biogenesis and protein degradation pathways, acting to balance rates of protein synthesis and breakdown.

The previously described effects of cellular growth and environmental conditions on nucleolar morphology and ribosome synthesis are reflected here by the large-scale and specific changes in the nucleolar proteome in response to distinct metabolic inhibitors. These data provide a more detailed and quantitative insight into how the cellular response to environmental stress and growth conditions affect the nucleolus. Further experiments will therefore be focused on the cause and effect of the relocalization of individual nucleolar proteins under these perturbations, and how these redistributions can orchestrate the regulation of cell growth and proliferation.

This study establishes a quantitative approach for the high-throughput characterization of the flux of endogenous proteins through cellular organelles, demonstrated here for the nucleolus. It will be important to study the dynamic nature of other subcellular structures, compartments and organelles because it is likely that their protein compositions can also vary extensively under different growth and/or metabolic conditions. We conclude that there is no unique, complete proteome for the nucleolus, or probably for any other organelle, but rather an overlapping set of proteomes that are relevant to different cell states or conditions. □

Methods

Isolation of stable isotope-labelled nucleolar proteins

Cells were grown for at least five cell divisions in L-arginine-, L-arginine $^{13}C_6$ $^{14}N_4$-, or L-arginine $^{13}C_6$ $^{15}N_4$-labelling media before drug treatment[18]. Actinomycin D (5 mg ml^{-1} stock solution in EtOH) was added at a final concentration of 1 μg ml^{-1} to Arg6- and Arg10-labelled cells and incubated for 20 and 80 min, respectively. The experiment was repeated with drug treatment for 40 and 160 min of Arg6- and Arg10-labelled cells, respectively, to give a total of five time points with untreated Arg0 cells as a common zero time point. In independent experiments, cells were treated with actinomycin D to give a total of nine time points, and with the proteasome inhibitor MG132 (10 μM for 1, 4, 8 and 16 h) and the polymerase II inhibitor DRB (25 μg ml^{-1} for 2 h and mock treated).

Nucleoli were isolated from HeLa cells or from a 1:1:1 mixture of Arg0, Arg6 and Arg10 HeLa$^{YFP–p68}$ cells as previously described[6] (http://www.lamondlab.com/f5nucleolarprotocol.htm). Isolated nucleolar proteins were separated on NuPAGE 4–12% Bis-Tris gel and excised into 16–20 slices. Peptides resulting from in-gel digestion were extracted from the gel pieces, desalted and concentrated on reverse-phase C18 tips, and eluted into 96-well plates for automated mass spectrometry analysis.

Western blots were performed with an antibody against p68 (gift from R. Janknecht), which recognized both the YFP-tagged and untagged forms of p68 (Fig. 4a) and an antibody against fibrillarin (gift from F. Fuller-Pace).

Mass spectrometry and data analysis

Mass spectrometric analysis was performed by liquid chromatography (Agilent HP1100) combined with tandem mass spectrometry (LC MS/MS) using a quadrupole time-of-flight instrument (QSTAR-XL, ABI-MDS-Sciex) or a linear ion-trap Fourier-transform ion-cyclotron resonance mass spectrometer (LTQ-FT-ICR, Thermo-Finnigan). For the QSTAR-XL, precursor ion spectra (m/z 350–1,500) and product ion spectra (m/z 70–1,500) of the four most intense ions were collected for 1 s. The LTQ-FT-ICR instrument was operated in the data-dependent mode to acquire high-resolution precursor ion spectra (m/z 300–1,500, $R = 25{,}000$ and ion accumulation to a target value of 10,000,000) in the ICR cell. The three most intense ions were sequentially isolated for accurate mass measurements by selected ion monitoring (SIM) scans (10 Da mass window, $R = 50{,}000$, and a target accumulation value of 50,000). The ions were simultaneously fragmented in the linear ion trap with a normalized collision energy setting of 27% and a target value of 2,000.

Stringent criteria were required for protein identification in the International Protein Index database using the Mascot program (Matrix Science) and LTQ-FT-ICR data: at least two matching peptides per protein, a mass accuracy within 3 p.p.m. (average absolute peptide mass accuracy was 0.7 p.p.m.), a Mascot score for individual peptides of better than 20, and a delta score of better than 5. Experiments with a reversed database[26] indicated that, under these conditions, proteins with two matching peptides were identified with a false positive rate of less than 0.1 per cent.

Protein ratios were calculated for each arginine-containing peptide as the peak area ratio of Arg6/Arg0 and Arg10/Arg0 of each single scan mass spectrum. The peptide ratios were averaged for all arginine-containing peptides sequenced for each protein and normalized to zero ($x - 1$). Normalized inverted ratios were calculated for ratios smaller than one [$1 - (1/x)$]. MS-Quant (http://msquant.sourceforge.net/), an in-house developed software program was used to evaluate the certainty in peptide identification and in peptide abundance ratio.

Live cell imaging

HeLa$^{YFP–p68}$ cells[8], HeLa YFP–FIB cells[27] and HeLa YFP–RPL27 cells[27] were cultured in Willco thin glass-bottomed microwell dishes (Intracel), mounted on a Deltavision Spectris microscope (Applied Precision) fitted in a transparent environmental chamber (Solent Scientific). Cells were imaged 60× (NA 1.4) Plan Apochromat objective. Twelve optical sections separated by 0.5 μm were recorded for each field and each exposure lasted for 0.05 s. After recording the first three time points, actinomycin D was added and cells were imaged for 2–3 h (SoftWoRx image processing software, Applied Precision). Nucleoli or nuclei (see Fig. 3) were outlined manually and five nucleoli/nuclei were measured from two independent experiments. In control experiments an equal volume of ethanol was added instead of actinomycin D.

Transcription assays

Briefly, isolated nucleoli were incubated with run-on buffer (100 mM KC1, 50 mM Tris–HCl pH 7.4, 5 mM $MgC1_2$, 0.5 mM EGTA, 0.5 mM ATP, 0.5 mM CTP, 0.5 mM GTP and 0.2 mM Br-UTP (Sigma Chemicals)) for 20 min at room temperature[28]. The

incubated nucleoli were spotted on a poly-L-lysine coated slide (BDH) then fixed in 2% paraformaldehyde (5 min, room temperature) and permeabilized in 0.5% Triton X-100 (10 min, room temperature), before being immunolabelled with anti-BrdU antibody (Sigma Chemicals), FITC-conjugated anti-mouse immunoglobulin (Jackson's lab) and counterstained with Pyronin Y (Sigma Chemicals). Transcription in intact HeLa cells was detected as reported[29]. Microscopy and image handling was performed using a Deltavision Spectris microscope as described above.

Received 18 October; accepted 16 November 2004; doi:10.1038/nature03207.

1. Visintin, R. & Amon, A. The nucleolus: the magician's hat for cell cycle tricks. *Curr. Opin. Cell Biol.* **12,** 752 (2000).
2. Guarente, L. Link between aging and the nucleolus. *Genes Dev.* **11,** 2449–2455 (1997).
3. Sherr, C. J. & Weber, J. D. The ARF/p53 pathway. *Curr. Opin. Genet. Dev.* **10,** 94–99 (2000).
4. Olson, M. O. Sensing cellular stress: another new function for the nucleolus? *Sci. STKE* [online] **pe10** (2004) (doi:10.1126/stke.2242004pe10).
5. Aebersold, R. & Mann, M. Mass spectrometry-based proteomics. *Nature* **422,** 198–207 (2003).
6. Mauramatsu, M., Smetana, K. & Busch, H. Quantitative aspects of isolation of nucleoli of the Walker carcinosarcoma and liver of the rat. *Cancer Res.* **25,** 693–697 (1963).
7. Huh, W. K. *et al.* Global analysis of protein localization in budding yeast. *Nature* **425,** 686–691 (2003).
8. Andersen, J. S. *et al.* Directed proteomic analysis of the human nucleolus. *Curr. Biol.* **12,** 1–11 (2002).
9. Trinkle-Mulcahy, L., Sleeman, J. E. & Lamond, A. I. Dynamic targeting of protein phosphatase 1 within the nuclei of living mammalian cells. *J. Cell Sci.* **114,** 4219–4228 (2001).
10. Li, D., Meier, U. T., Dobrowolska, G. & Krebs, E. G. Specific interaction between casein kinase 2 and the nucleolar protein Nopp140. *J. Biol. Chem.* **272,** 3773–3779 (1997).
11. Yamamoto, R. T., Nogi, Y., Dodd, J. A. & Nomura, M. RRN3 gene of *Saccharomyces cerevisiae* encodes an essential RNA polymerase I transcription factor which interacts with the polymerase independently of DNA template. *EMBO J.* **15,** 3964–3973 (1996).
12. Charroux, B. *et al.* Gemin4. A novel component of the SMN complex that is found in both gems and nucleoli. *J. Cell Biol.* **148,** 1177–1186 (2000).
13. Lamond, A. I. & Earnshaw, W. C. Structure and function in the nucleus. *Science* **280,** 547–553 (1998).
14. Misteli, T. Protein dynamics: implications for nuclear architecture and gene expression. *Science* **291,** 843–847 (2001).
15. Lamond, A. I. & Sleeman, J. E. Nuclear substructure and dynamics. *Curr. Biol.* **13,** R825–R828 (2003).
16. Leung, A. K. & Lamond, A. I. *In vivo* analysis of NHPX reveals a novel nucleolar localization pathway involving a transient accumulation in splicing speckles. *J. Cell Biol.* **157,** 615–629 (2002).
17. Ong, S. E. *et al.* Stable isotope labeling by amino acids in cell culture, SILAC, as a simple and accurate approach to expression proteomics. *Mol. Cell. Proteomics* **1,** 376–386 (2002).
18. Blagoev, B., Ong, S. E., Kratchmarova, I. & Mann, M. Temporal analysis of phosphotyrosine-dependent signaling networks by quantitative proteomics. *Nature Biotechnol.* **22,** 1139–1145 (2004).
19. Perry, R. P. & Kelley, D. E. Inhibition of RNA synthesis by actinomycin D: characteristic dose-response of different RNA species. *J. Cell. Physiol.* **76,** 127–139 (1970).
20. Raghavan, A. *et al.* Genome-wide analysis of mRNA decay in resting and activated primary human T lymphocytes. *Nucleic Acids Res.* **30,** 5529–5538 (2002).
21. Tschochner, H. & Hurt, E. Pre-ribosomes on the road from the nucleolus to the cytoplasm. *Trends Cell Biol.* **13,** 255–263 (2003).
22. Dragon, F. *et al.* A large nucleolar U3 ribonucleoprotein required for 18S ribosomal RNA biogenesis. *Nature* **417,** 967–970 (2002).
23. Eisen, M. B., Spellman, P. T., Brown, P. O. & Botstein, D. Cluster analysis and display of genome-wide expression patterns. *Proc. Natl Acad. Sci. USA* **95,** 14863–14868 (1998).
24. Tamm, I., Hand, R. & Caliguiri, L. A. Action of dichlorobenzimidazole riboside on RNA synthesis in L-929 and HeLa cells. *J. Cell Biol.* **69,** 229–240 (1976).
25. Mattsson, K., Pokrovskaja, K., Kiss, C., Klein, G. & Szekely, L. Proteins associated with the promyelocytic leukemia gene product (PML)-containing nuclear body move to the nucleolus upon inhibition of proteasome-dependent protein degradation. *Proc. Natl Acad. Sci. USA* **98,** 1012–1017 (2001).
26. Olsen, J. V., Ong, S. E. & Mann, M. Trypsin cleaves exclusively C-terminal to Arginine and lysine residues. *Mol. Cell. Proteomics* **6,** 608–614 (2004).
27. Leung, A. K. *et al.* Quantitative kinetic analysis of nucleolar breakdown and reassembly during mitosis in live human cells. *J. Cell Biol.* **166,** 787–800 (2004).
28. Masson, C. *et al.* Conditions favoring RNA polymerase I transcription in permeabilized cells. *Exp. Cell Res.* **226,** 114–125 (1996).
29. Boisvert, F. M., Hendzel, M. J. & Bazett-Jones, D. P. Promyelocytic leukemia (PML) nuclear bodies are protein structures that do not accumulate RNA. *J. Cell Biol.* **148,** 283–292 (2000).
30. Scherl, A. *et al.* Functional proteomic analysis of human nucleolus. *Mol. Biol. Cell* **13,** 4100–4109 (2002).

Supplementary Information accompanies the paper on **www.nature.com/nature**.

Acknowledgements We thank A. Fox for providing the HeLa$^{YFP-p68}$ cell line and other members of the Lamond and the Mann laboratories for help and discussions. Work in the Center for Experimental Bioinformatics (CEBI) is supported by a grant from the Danish National Research Foundation. A.I.L. is a Wellcome Trust Principal Research Fellow and is funded by a Wellcome Trust Programme grant; A.K.L.L. was funded by a Croucher studentship; Y.W.L. was funded by The Human Frontier Science Program, which is also acknowledged for a network grant entitled 'Functional organization of the cell nucleus investigated through proteomics and molecular dynamics'.

Competing interests statement The authors declare that they have no competing financial interests.

Correspondence and requests for materials should be addressed to A.I.L. (a.i.lamond@dundee.ac.uk) or M.M. (mann@bmb.sdu.dk).

Vitamin C degradation in plant cells via enzymatic hydrolysis of 4-*O*-oxalyl-L-threonate

Martha A. Green & Stephen C. Fry

The Edinburgh Cell Wall Group, Institute of Molecular Plant Sciences, School of Biological Sciences, The University of Edinburgh, Daniel Rutherford Building, The King's Buildings, Edinburgh EH9 3JH, UK

Increasing the L-ascorbate (vitamin C) content of crops could in principle involve promoting its biosynthesis or inhibiting its degradation. Recent progress has revealed biosynthetic pathways for ascorbate[1–3], but the degradative pathways remain unclear. The elucidation of such pathways could promote an understanding of the roles of ascorbate in plants[4], and especially of the intriguing positive correlation between growth rate and ascorbate oxidase[5,6] (or its products[7]). In some plants (Vitaceae), ascorbate is degraded via L-idonate to L-threarate (L-tartrate), with the latter arising from carbons 1–4 of ascorbate[3,8–11]. In most plants, however (including Vitaceae)[11], ascorbate degradation can occur via dehydroascorbate, yielding oxalate[12] plus L-threonate, with the latter from carbons 3–6 of ascorbate[3,10,13]. The metabolic steps between ascorbate and oxalate/L-threonate, and their subcellular location, were unknown. Here we show that this pathway operates extracellularly in cultured *Rosa* cells, proceeds via several novel intermediates including 4-*O*-oxalyl-L-threonate, and involves at least one new enzyme activity. The pathway can also operate non-enzymatically, potentially accounting for vitamin losses during cooking. Several steps in the pathway may generate peroxide; this may contribute to the role of ascorbate as a pro-oxidant[14,15] that is potentially capable of loosening the plant cell wall and/or triggering an oxidative burst.

A significant proportion of a plant's ascorbate is found in the apoplast (the aqueous solution permeating the cell walls)[6,16]. To investigate the degradation of apoplastic ascorbate, we fed 0.5 mM L-[1-^{14}C]ascorbate to *Rosa* cell-suspension cultures. Extracellular ascorbate steadily disappeared, at a rate that was greatest in fast-growing cell cultures. In 5-day-old cultures, the initial rate of ascorbate degradation was $\sim$10 μM min^{-1}. Over 90% of the ^{14}C remained in the medium for the first 5 h, indicating extracellular metabolism rather than uptake by cells or loss as $^{14}CO_2$.

L-[1-^{14}C]Ascorbate incubated with 5-day-old cultures yielded at least seven radioactive products (**A**–**G**), resolved by electrophoresis at pH 6.5 (see Fig. 4). The mobilities of these products relative to the marker Orange G (m_{OG} values) were: **A**, 0.00; **B**, 1.25; **C**, 1.38; **D**, 1.42; **E**, 1.96; **F**, 2.32; **G**, 3.15; and ascorbate, 1.01 (mean values from five electrophoretograms). m_{OG} is proportional to the ratio of a molecule's charge (Q) to its surface area (represented by $M_r^{2/3}$, ref. 17).

A and **B** were identified by comparison with markers as dehydroascorbate and 2,3-diketogulonate respectively; these are well-known ascorbate degradation products. On electrophoresis at pH 6.5 and 2.0, **G** co-migrates with oxalate. Its high mobility at pH 2.0 ($m_{OG} \approx 1.1$) is particularly characteristic of oxalate, whose first pK_a ($\approx$1.25) is unusually low.

F is a novel compound. At pH 6.5, it migrates between L-threarate and erythrarate (*meso*-tartrate), suggesting that **F** also has two negatively charged groups. At pH 2.0, its m_{OG} (0.83) is much higher than that for threarate (0.11) or erythrarate (0.08), showing that **F** has a low pK_a.

Alkali rapidly hydrolysed ^{14}C-**F** to [^{14}C]oxalate (Fig. 1b) plus a non-radioactive product co-electrophoresing with L-threonate (Fig. 1a). High-pressure liquid chromatography (HPLC) showed